Science Advances
AAAS

Supplementary Materials for

At-home wireless sleep monitoring patches for the clinical assessment of sleep quality and sleep apnea

Shinjae Kwon *et al.*

Corresponding author: Woon-Hong Yeo, whyeo@gatech.edu

Sci. Adv. **9**, eadg9671 (2023)
DOI: 10.1126/sciadv.adg9671

The PDF file includes:

Other Supplementary Material for this manuscript includes the following:

Note S1 | Derivation of conformal contact model of electrode and silicone elastomer with stiff backing layer on microstructure of skin

To make a mechanical model of contact of system on microstructure of skin, the interface between the system and skin is analytically modeled. The microscopic morphology of the skin surface is assumed to be sinusoidal, and modeled as:

$$y(x) = \frac{h_{rough}}{2}\left(1 + \frac{\cos(2\pi x)}{\lambda_{rough}}\right) \quad (1)$$

In equation (1), h_{rough} is the amplitude, and λ_{rough} is the wavelength of the sinusoidal model of the skin. When the system makes conformal contact with skin, both the system and the skin undergo deformation to create equilibrium sinusoidal morphology with altered amplitude, but with the same wavelength. In this model, the maximum deflection of the electrode, or the new amplitude of the sinusoid, is noted as h. Displacement undergone by the electrode and skin are modeled as:

$$w(x) = \frac{h}{2}\left(1 + \frac{\cos(2\pi x)}{\lambda_{rough}}\right) \quad (2)$$

$$u_z(x) = y - w = \frac{h_{rough} - h}{2}\left(1 + \frac{\cos(2\pi x)}{\lambda_{rough}}\right) \quad (3)$$

In prior works with skin-conformable electronics, the conformality of the system was determined by deriving the interfacial contact energy ($U_{conformal}$) of the system and skin, which is the sum of three different energies, expressed as:

$$U_{conformal} = U_{bending} + U_{skin} + U_{adhesion} \quad (4)$$

In this equation (4), $U_{bending}$, U_{skin}, and $U_{adhesion}$ represent bending energy of electrode, elastic energy of skin, and contact adhesion energy between the system and skin, respectively. The prior works that used this three-energy model made a major assumption that the entire system behaves as an ultrathin film, and the entire system deforms conformally to that of skin. Bending energy in the three-energy model includes the energy required to bend both the electrode and the supporting silicone elastomer layer. On the other hand, in our new system, it is assumed that the ultrasoft silicone elastomer used, Silbione, undergo normal deformation, rather than bending, to compensate the interface between the flat, rigid surface of the relatively stiff fabric backing layer

and the curvilinear, sinusoidal surface of the skin. This new interface is modeled with four-energy as:

$$U_{conformal} = U_{bending} + U_{silicone} + U_{skin} + U_{adhesion} \qquad (5)$$

In this new four-energy interfacial model presented in equation (5), $U_{bending}$ represents the bending energy of the electrode alone, and $U_{silicone}$ represents the elastic deformation energy of the silicone elastomer. In both previous and new model, non-conformal contact is defined as a state where no component experiences any deformation. Therefore, non-conformal contact is defined as a state where the total energy is zero, $U_{non\text{-}conformal}=0$. The electrode bending energy is modeled as:

$$U_{bending} = \frac{1}{\lambda_{rough}} \int_0^{\lambda_{rough}} \frac{\alpha EI_{electrode}(w")^2}{2} dx = \frac{\alpha \pi^4 EI_{electrode} h^2}{\lambda_{rough}^4} \qquad (6)$$

In this bending energy model in equation (6), α is areal fraction, or fill-factor, of the mesh-patterned electrode. The effective bending stiffness of the electrode, $EI_{electrode}$, is determined as:

$$EI_{electrode} = \sum_{i=1}^{N} E_i h_i \left[\left(b - \sum_{j=1}^{i} h_j \right)^2 + \left(b - \sum_{j=1}^{i} h_j \right) h_i + \frac{1}{3} h_i^2 \right] \qquad (7)$$

$$\text{where} \quad b = \sum_{i=1}^{N} E_i h_i \left(\sum_{j=1}^{i} h_j - \frac{1}{2} h_i \right) / \sum_{i=1}^{n} E_i h_i \qquad (8)$$

The effective bending stiffness of the electrode is modeled as a composite of *N* layers. E_i is the Young's modulus, and h_i is the thickness of the i^{th} layer.

The elastic deformation energy of silicone elastomer is modeled as:

$$U_{silicone} = \frac{1}{\lambda_{rough}} \int_0^{\lambda_{rough}} \frac{E_{silicone}(w)^2}{2t_{silicone}^2} dx = \frac{E_{silicone} h^2}{16 t_{elastomer}^2} \qquad (9)$$

In the model presented in equation (9), $E_{silicone}$ and $t_{silicone}$ represent the Young's modulus and thickness of the silicone elastomer, respectively.

Similarly with the previous works, the skin is modeled as a semi-infinite body subject to the surface displacement. The normal stress existing on the surface of the skin is analytically modeled as:

$$\sigma_z = \frac{\pi E_{skin}(h_{rough}-h)}{2\lambda_{rough}} \cos\left(\frac{2\pi x}{\lambda_{rough}}\right) \quad (10)$$

E_{skin} represents the Young's modulus of the skin. With the normal stress model in equation (10), the elastic energy of the skin can be derived as:

$$U_{skin} = \frac{1}{\lambda_{rough}} \int_0^{\lambda_{rough}} \frac{\sigma_z u_z}{2} dx = \frac{\pi E_{skin}(h_{rough}-h)^2}{16\lambda_{rough}} \quad (11)$$

The interfacial contact adhesion energy can be derived by multiplying work of adhesion (γ) with the contact area. In this case, the contact area of silicone on skin is reduced by the areal fraction. The adhesion energy is modeled as:

$$U_{adhesion} = -(1-\alpha)\gamma \int_0^{\lambda_{rough}} \sqrt{1+(w')^2}\, dx \approx -(1-\alpha)\gamma\left(1+\frac{\pi^2 h^2}{4\lambda_{rough}^2}\right) \quad (12)$$

Through minimization of total energy $\left(\frac{\partial U_{conformal}}{\partial h}\right)$ with respect to the maximum deflection (h) of electrode and skin, the value of h can be derived as:

$$h = \frac{\pi E_{skin} h_{rough}}{\frac{16\alpha\pi^4 EI_{electrode}}{\lambda_{rough}^3} + \frac{\lambda_{rough} E_{silicone}}{t_{silicone}^2} + \pi E_{skin}} \quad (13)$$

To achieve conformal contact, $U_{conformal}$ of the system should be larger than $U_{non\text{-}conformal}$. In other words, the adhesion energy should be larger than the sum of bending energy of electrode, elastic energy of silicone, and elastic energy of skin. Therefore, the condition to achieve conformal contact can be derived as:

$$(1-\alpha)\gamma\left(1+\frac{\pi^2 h^2}{4\lambda_{rough}^2}\right) > \left(\frac{\alpha\pi^4 EI_{electrode} h^2}{\lambda_{rough}^4} + \frac{E_{silicone} h^2}{16 t_{elastomer}^2} + \frac{\pi E_{skin}(h_{rough}-h)^2}{16\lambda_{rough}}\right) \quad (14)$$

In this study, the skin parameter values used are E_{skin} = 130 kPa, λ_{rough} = 385 μm, and h_{rough} = 55 μm. The areal fraction of the electrode α is 0.2687.

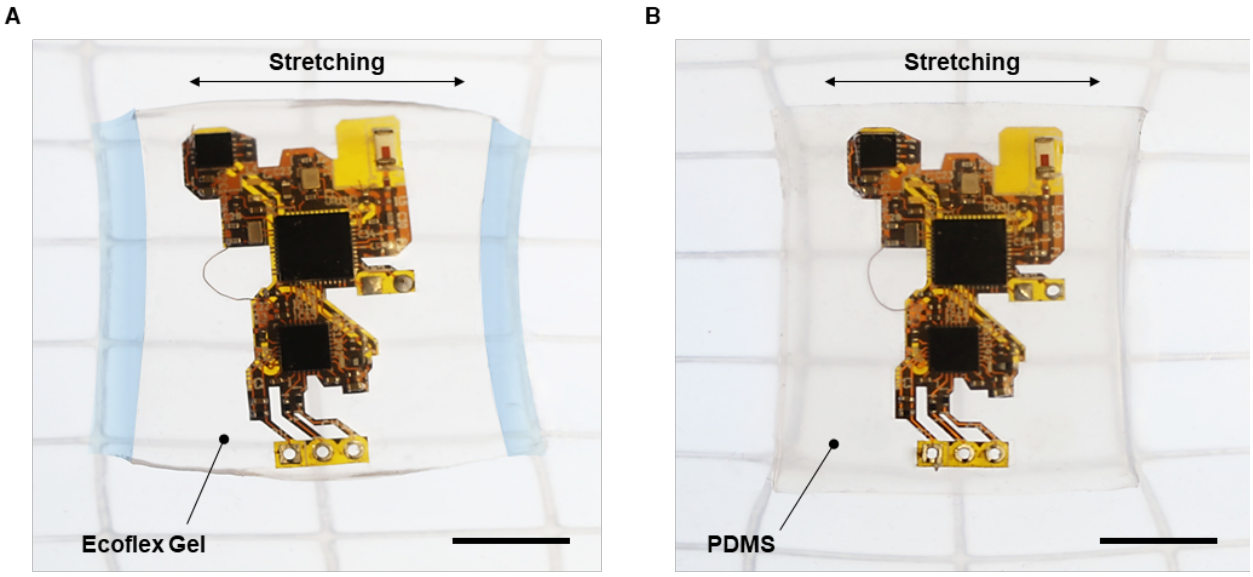

Fig. S1 | Strain isolation. Images of stretched the circuit with (**A**) or without (**B**) strain isolation layer. Low modulus Ecoflex Gel layer reduces the stress of the circuit by releasing its stress to proper strain. Scale bars, 1 cm.

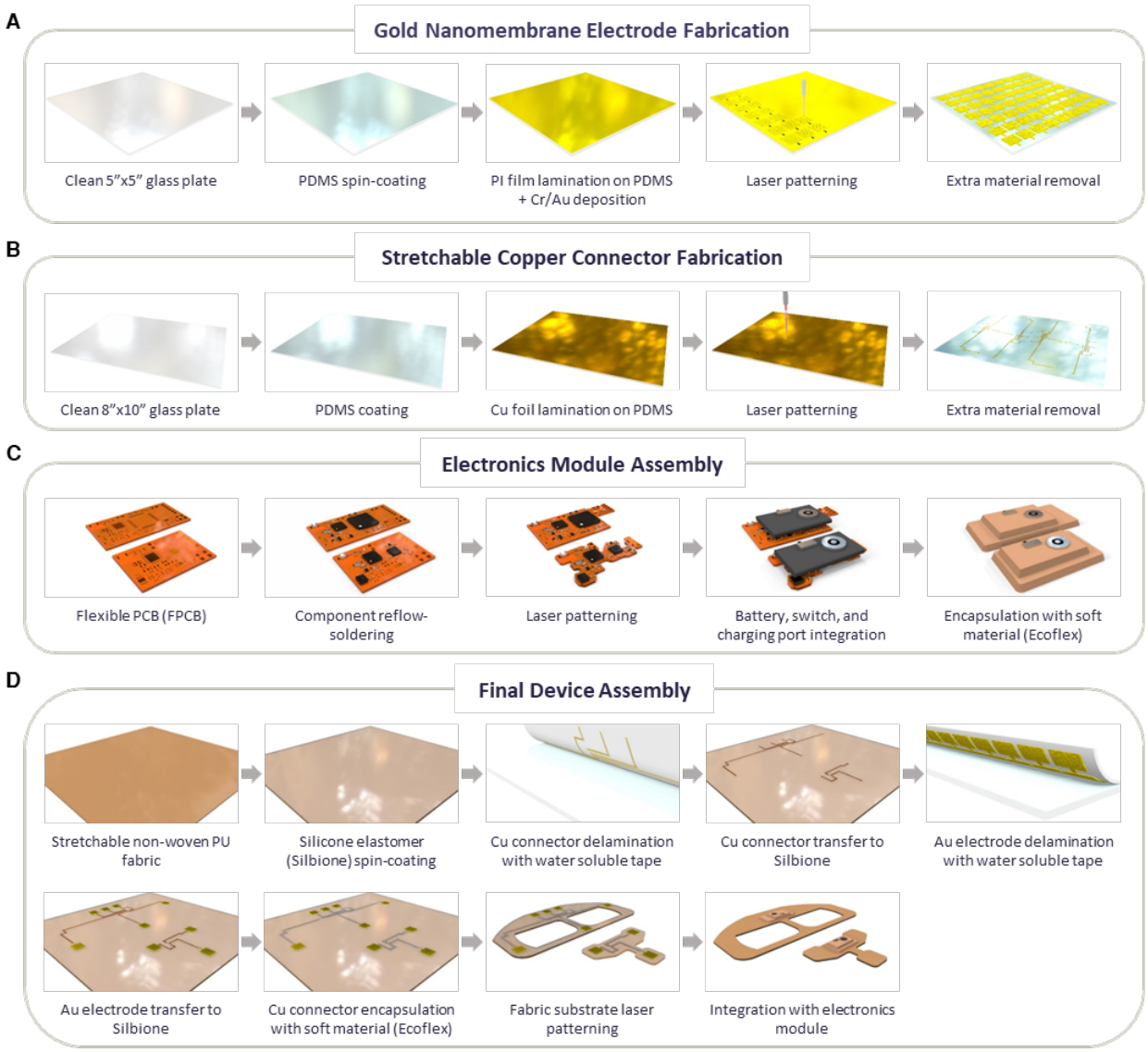

Fig. S2 | Schematic illustration of fabrication and assembly process of the devices. Fabrication process of the (**A**) Au nanomembrane mesh electrode and (**B**) stretchable, solderable Cu connector. (**C**) Integration of electronics and packaging process with soft material. (**D**) Fabrication of the fabric substrate and final device assembly process.

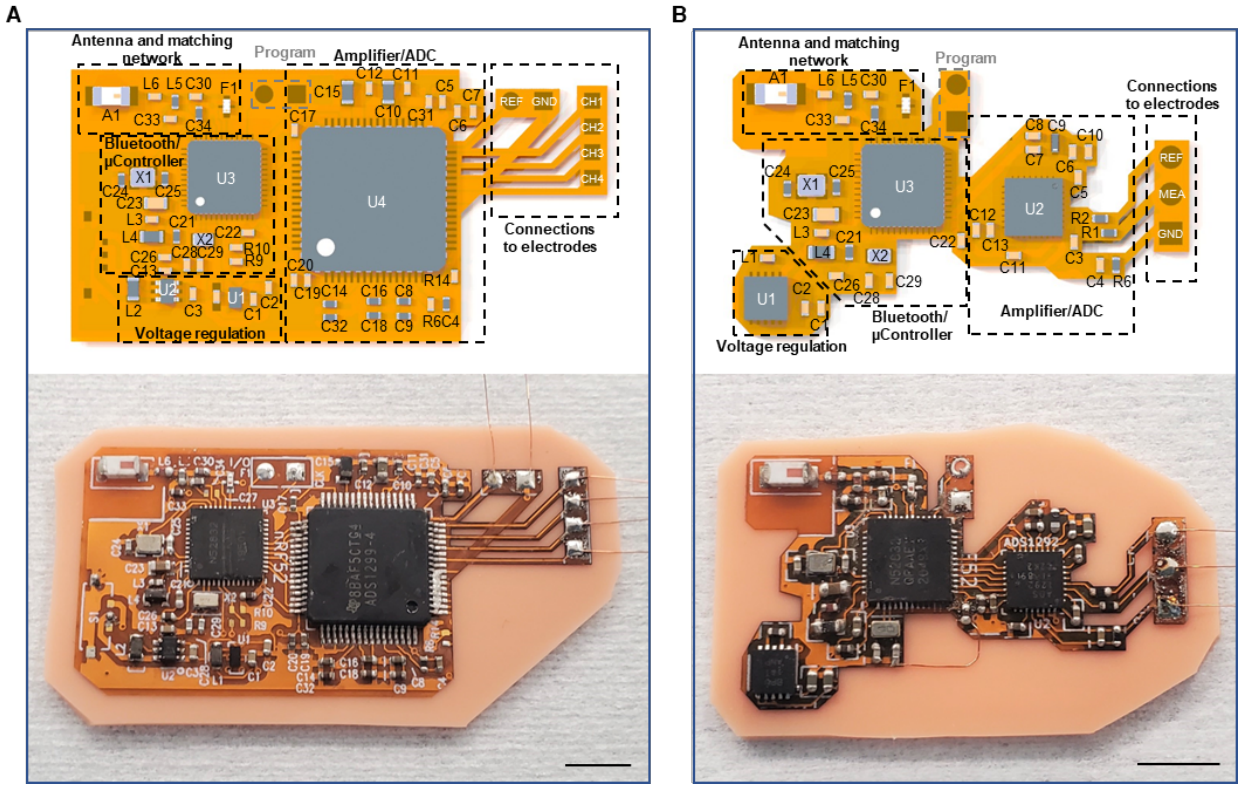

Fig. S3 | Circuit design. Top-view illustration of circuit component with highlighted functional blocks (top) and photo of the fully assembled FPCB (bottom) of system's (**A**) forehead unit and (**B**) chin unit. Scale bars, 5mm.

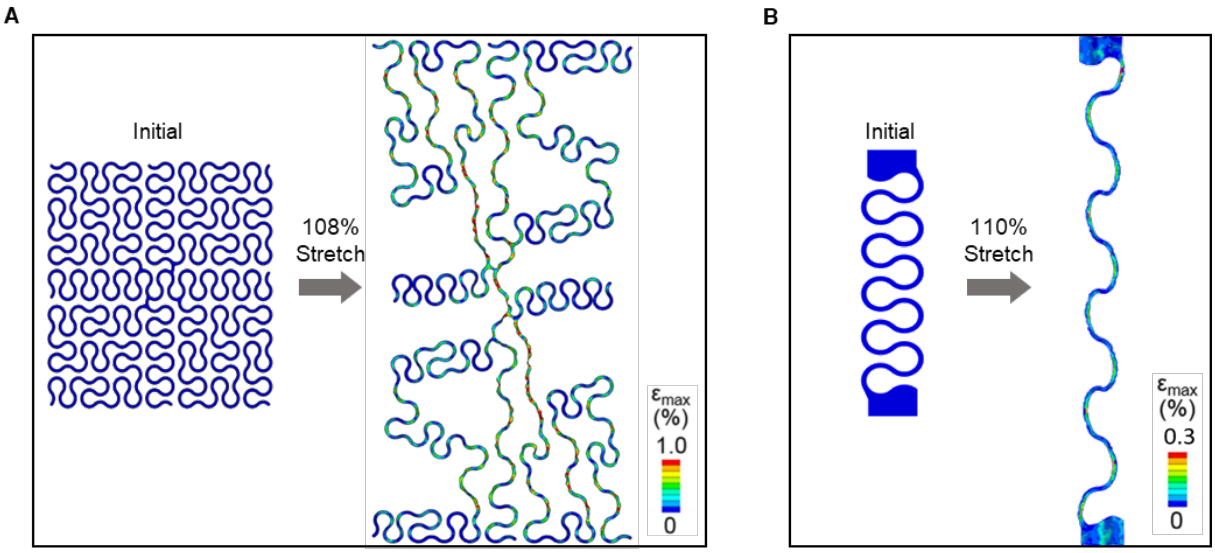

Fig. S4 | Stretching FEA up to fracture and yield of gold electrode and copper connector. FEA results of (**A**) gold electrode and (**B**) copper connector stretching up to the point where their local maximum strain value reaches their fracture (1%) and yield (0.3%) points, respectively.

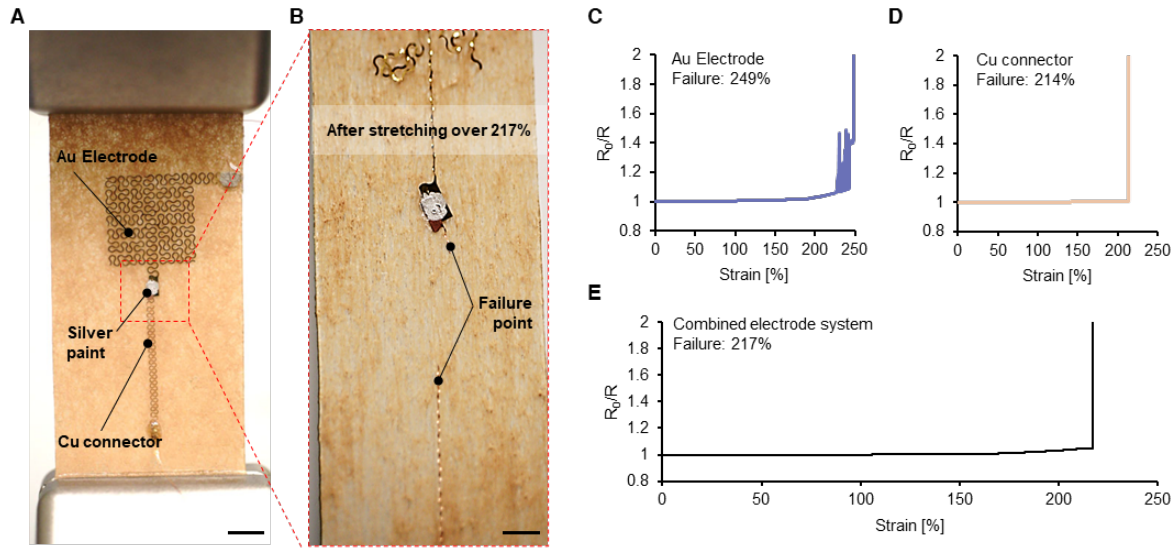

Fig. S5 | Mechanical/electrical failure evaluation of the Au electrode, Cu connector, and combined system. (**A**) Image of combined system. Silver paint allows a stable mechanical/electrical connection between Au electrode and Cu connector. Scale bars, 500 μm. (**B**) Cu connector failed over 217% strain. Scale bars, 300 μm. (**C**-**E**) Resistance change of the Au electrode, Cu connector, combined electrode system. (**C**) Au electrode failure point: 249% stretching, (**D**) Cu connector failure point: 214% (**E**) Combined system failure point: 217%. Cu connectors show lower maximum stretching stability, making the combined system follow the breakage point of the Cu connection.

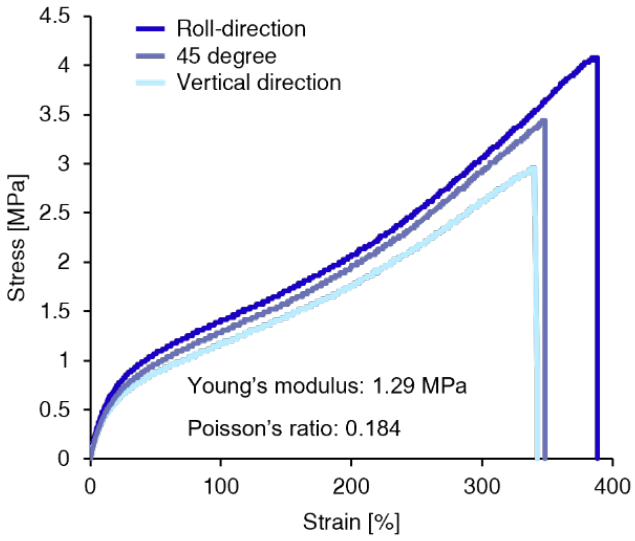

Fig. S6 | Mechanical characterization of the omnidirectional elasticity of the non-woven PU fabric. The strain-stress curves of the fabric stretched in three different directions up to failure, showing a nearly uniform result from all three directions. Calculated and averaged Young's modulus of the fabric is 1.29 MPa and Poisson's ratio is 0.128.

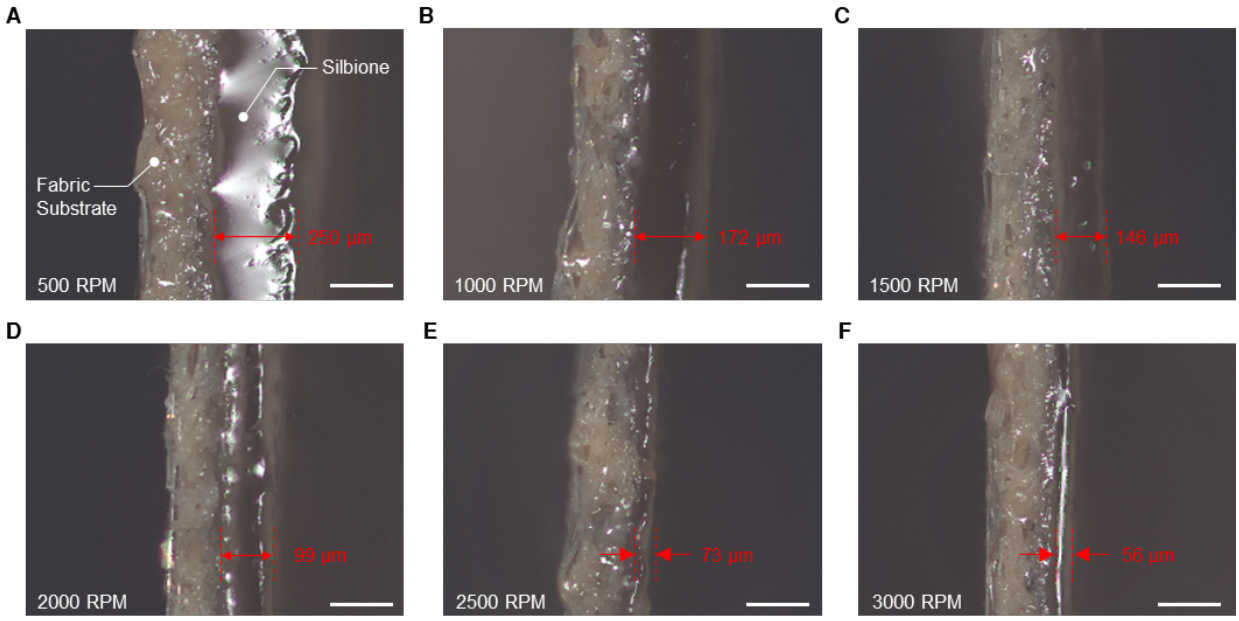

Fig. S7 | Silbione thickness with various spin coating conditions. (**A-F**) Thickness of fabric substrate: 250 μm, Thickness of Silbione: 250, 172, 146, 99, 73, 56 μm with spin coating with 500, 1000, 1500, 2000, 2500, 3000 RPM, respectively. Scale bars, 200 μm

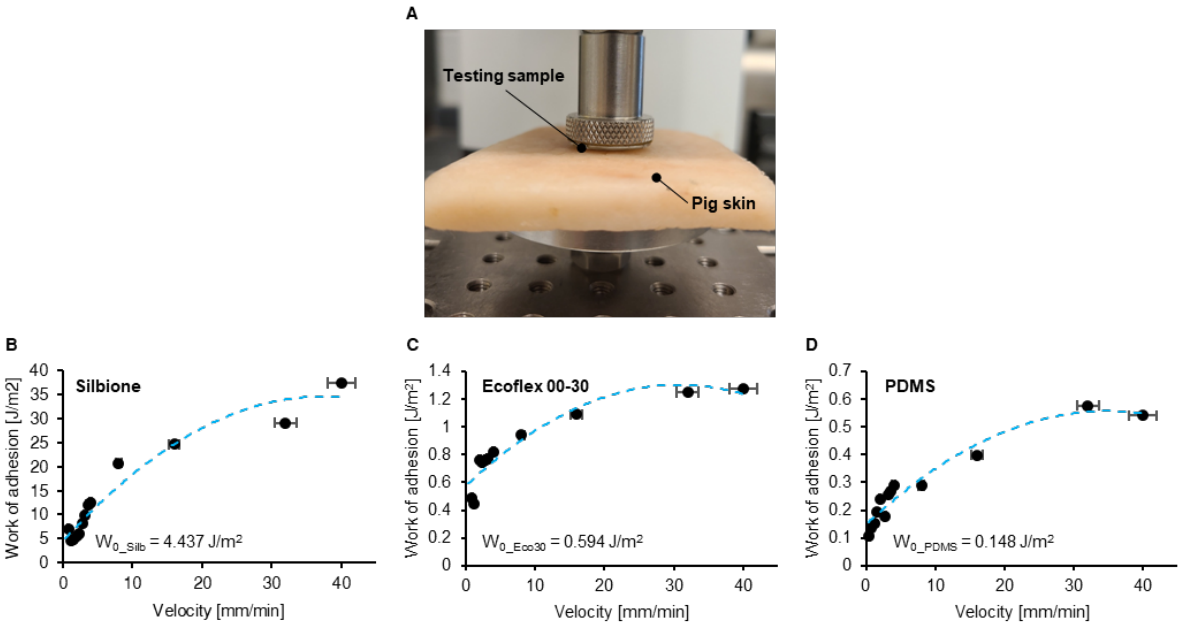

Fig. S8 | Determination of work of adhesion. (**A**) Photo of the test setup, (**B**-**D**) Curve fit lines and their work of adhesion values for Silbione, Ecoflex 00-30, PDMS.

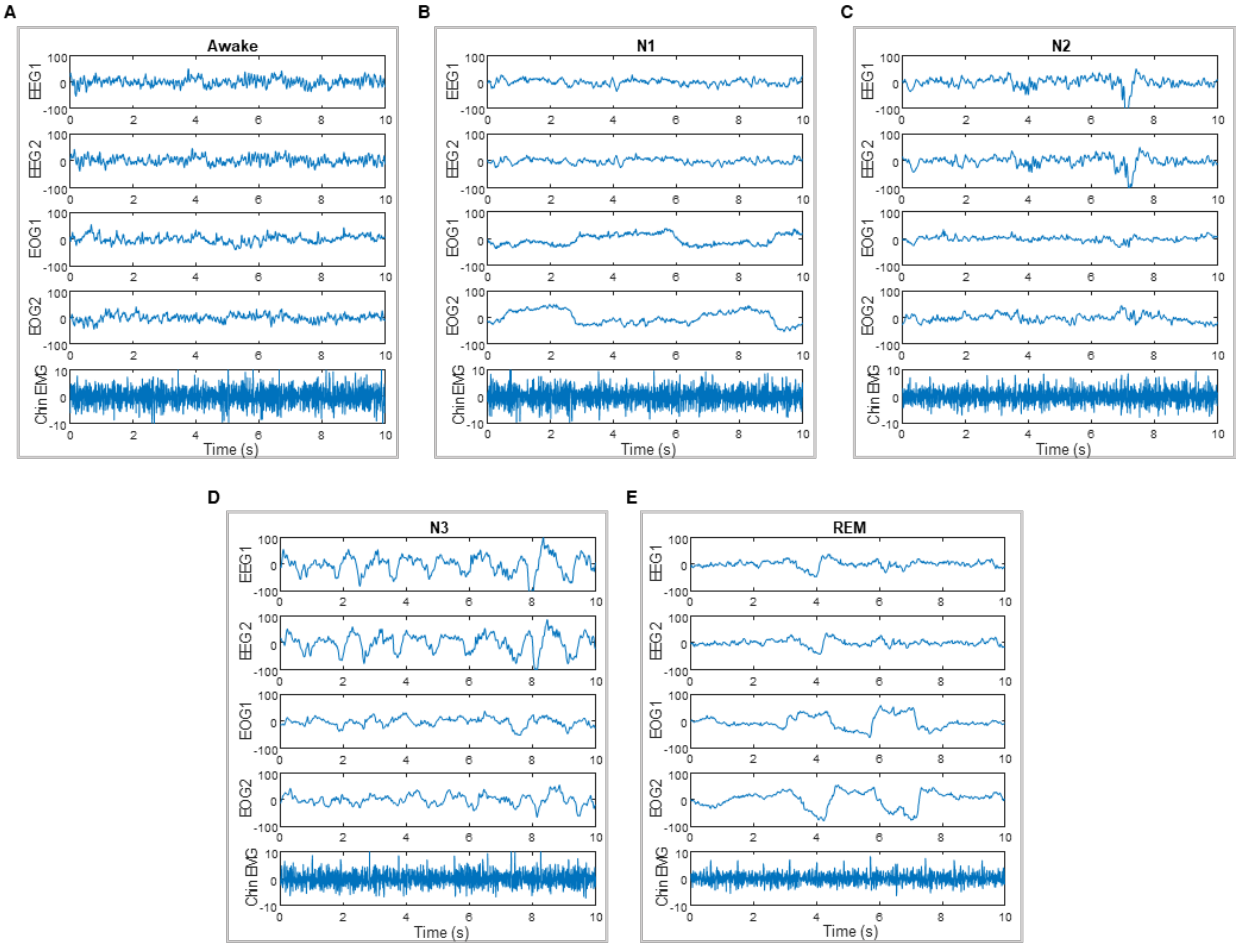

Fig. S9 | Representative signals from all five channels of the devices at each sleep stage. 10-second sample plots raw signals measured from all five channels of the devices capturing characteristic signals of each of the five sleep stages: (**A**) Awake, (**B**) Non-REM 1, (**C**) Non-REM 2, (**D**) Non-REM 3, and (**E**) REM. Y-axis unit is in microvolt (μV).

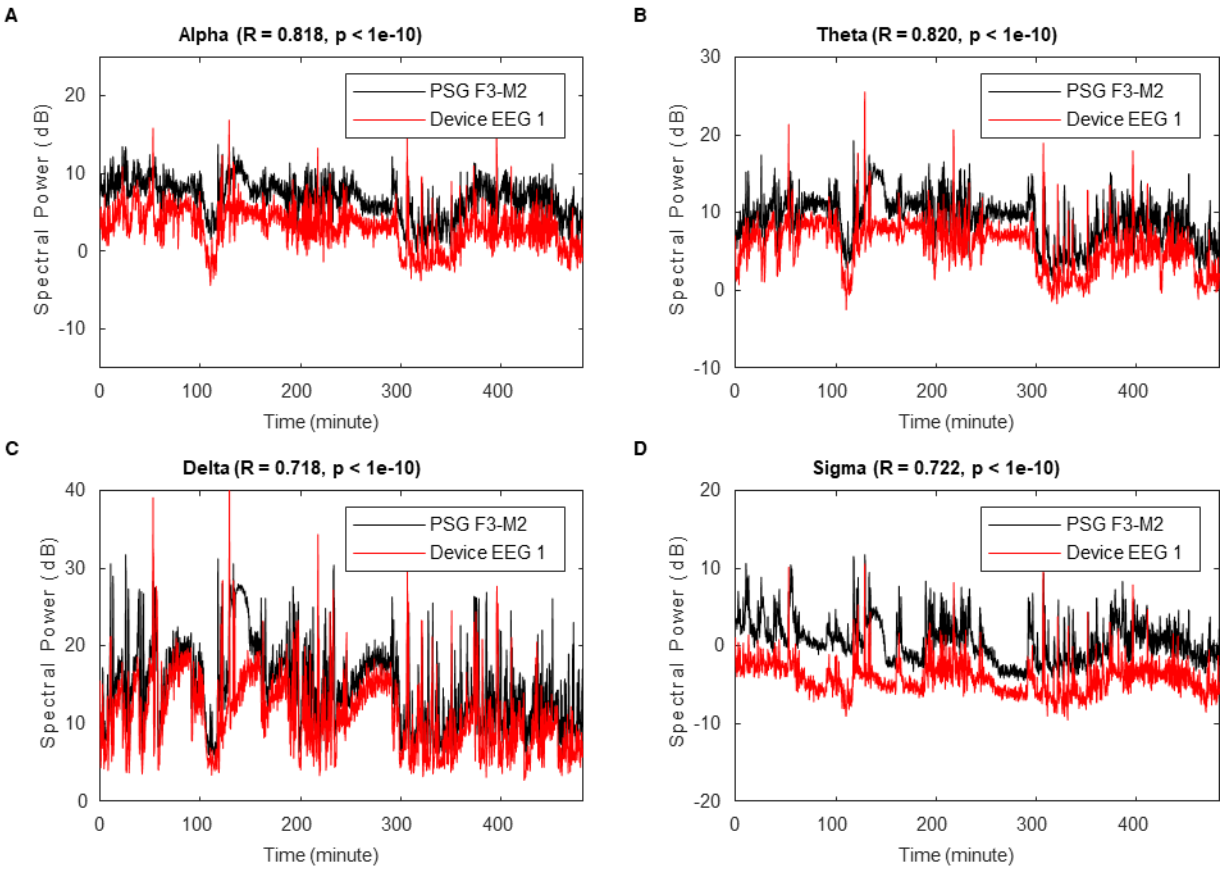

Fig. S10 | Spectral power comparison of EEG signals from PSG and our system. Plots comparing spectral powers of F3-M2 channel of PSG and EEG 1 channel of the device simultaneously measured from the same subject over the four main EEG frequency band: (**A**) alpha, (**B**) theta, (**C**) delta, and (**D**) sigma.

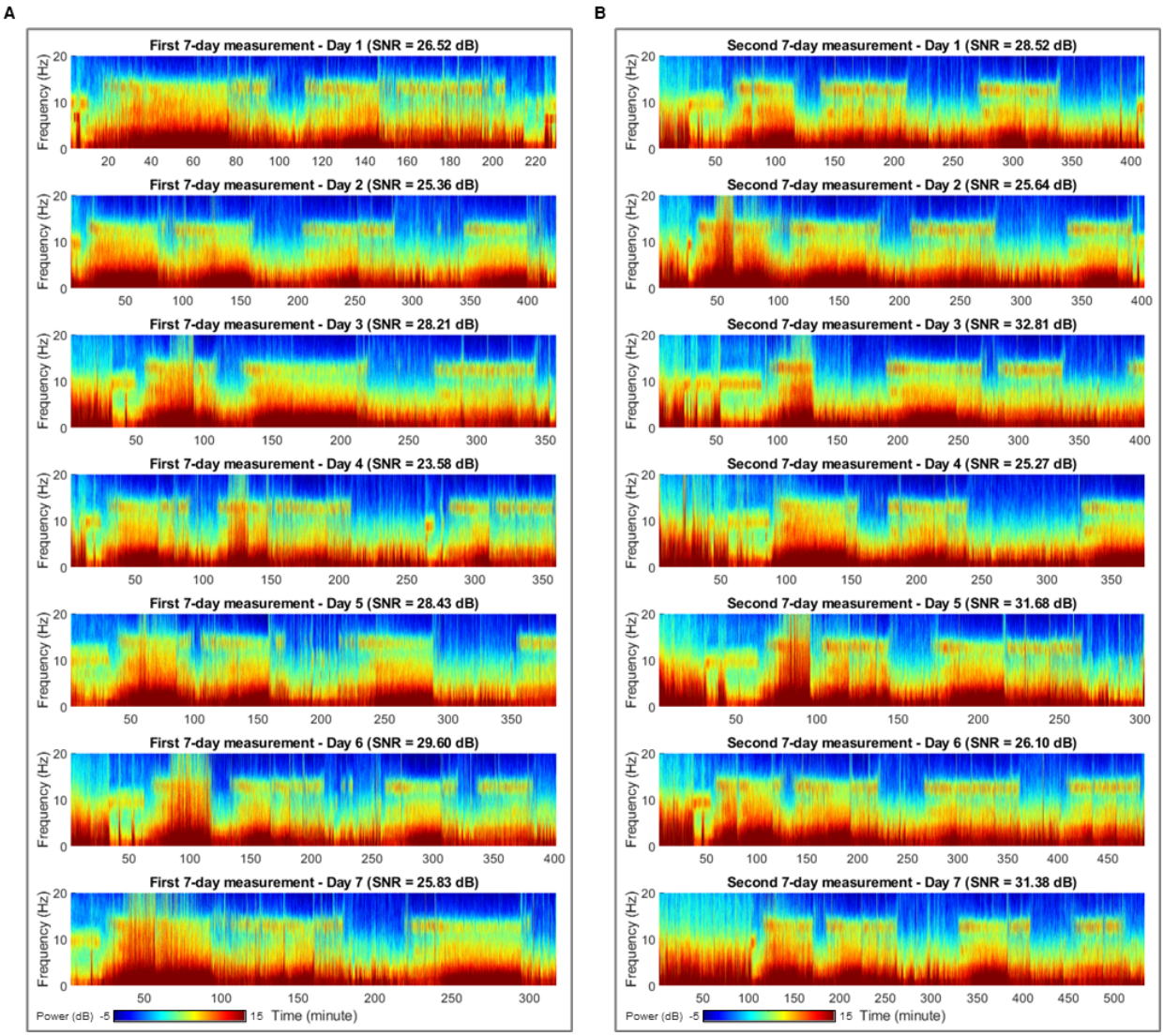

Fig. S11 | Spectrograms of seven consecutive sleep measurements. Seven spectrograms generated from EEG1 signals at each day of seven consecutive sleep measurements with our system during the (**A**) first week and (**B**) second week of the whole measurement, showing a negligible change in the signal strengths and the calculated SNR values of the delta wave during N3 stages.

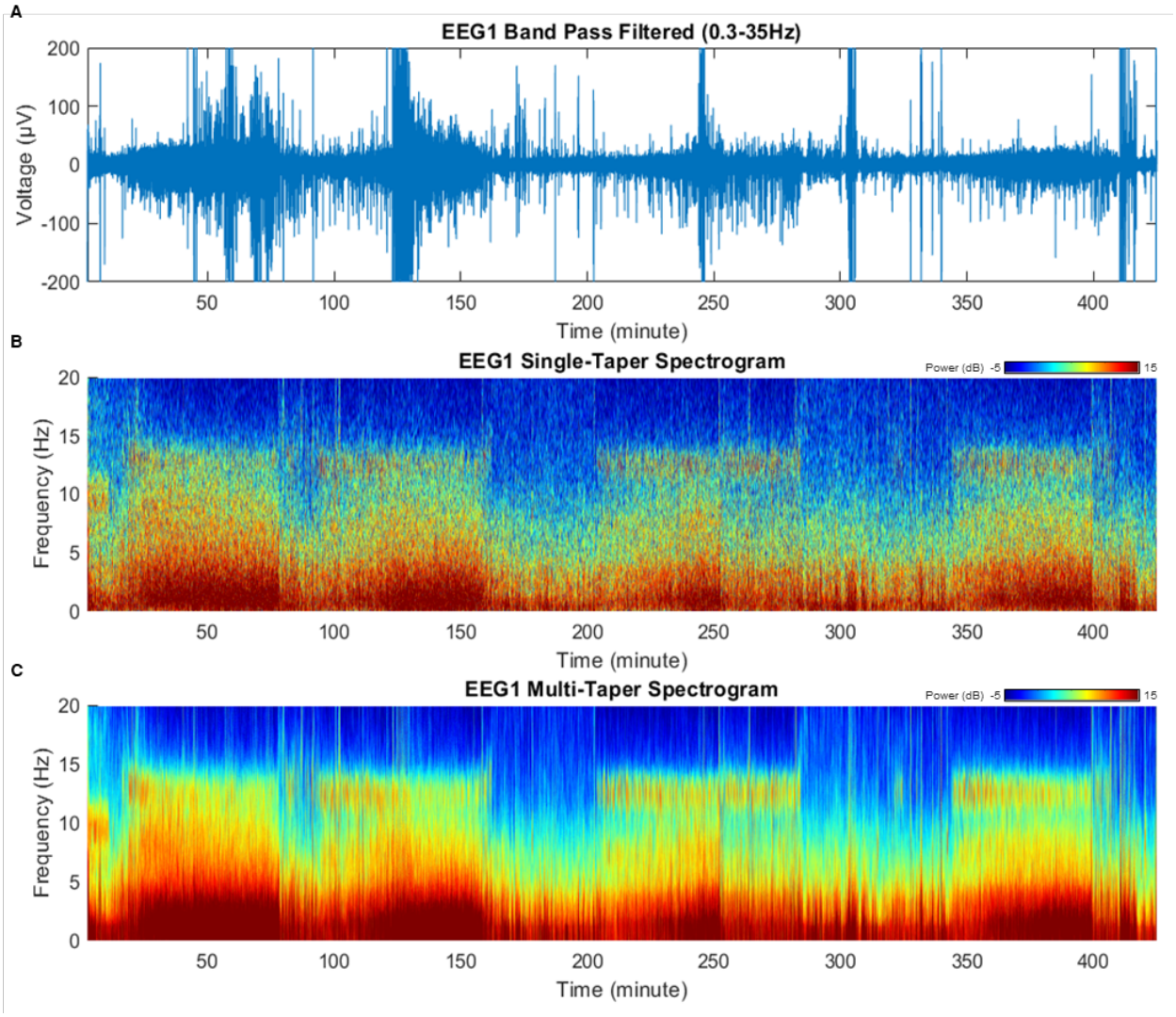

Fig. S12 | Comparison of single- and multi-taper spectrogram. Plots showing and comparing (**A**) band pass-filtered raw EEG 1 signals, (**B**) standard single-taper spectrogram, and (**C**) multi-taper spectrogram that features higher clarity with minimized bias and variance in spectral estimation.

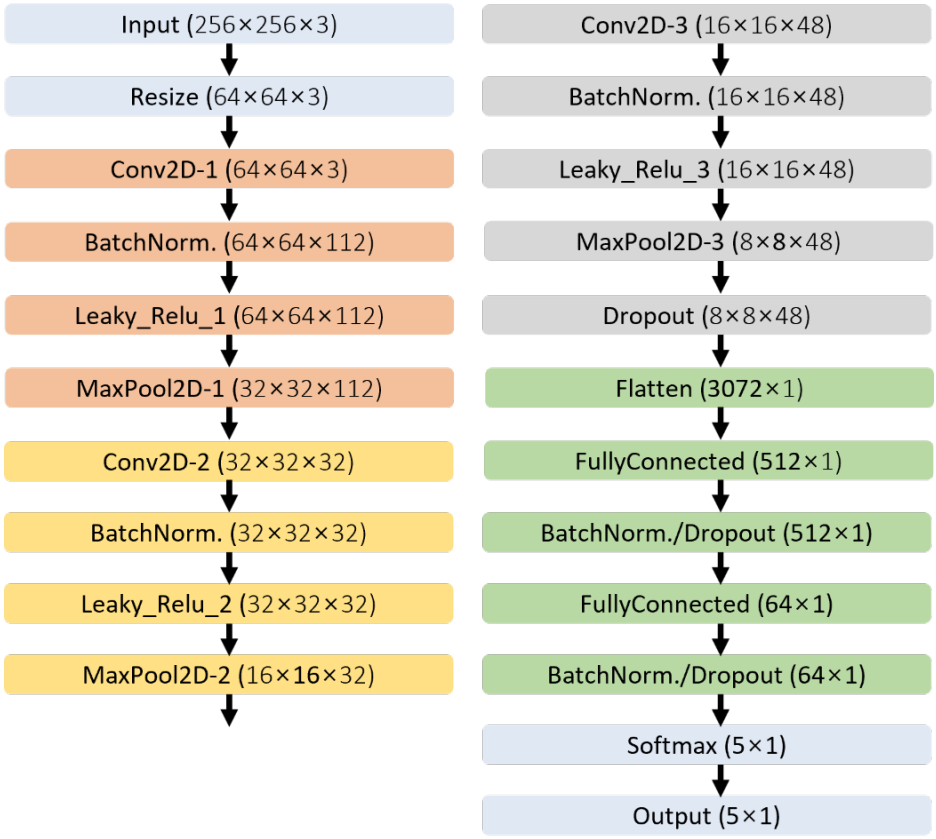

Fig. S13 | Machine learning architecture for sleep stage classification. The architecture of proposed deep neural network for sleep stage classification.

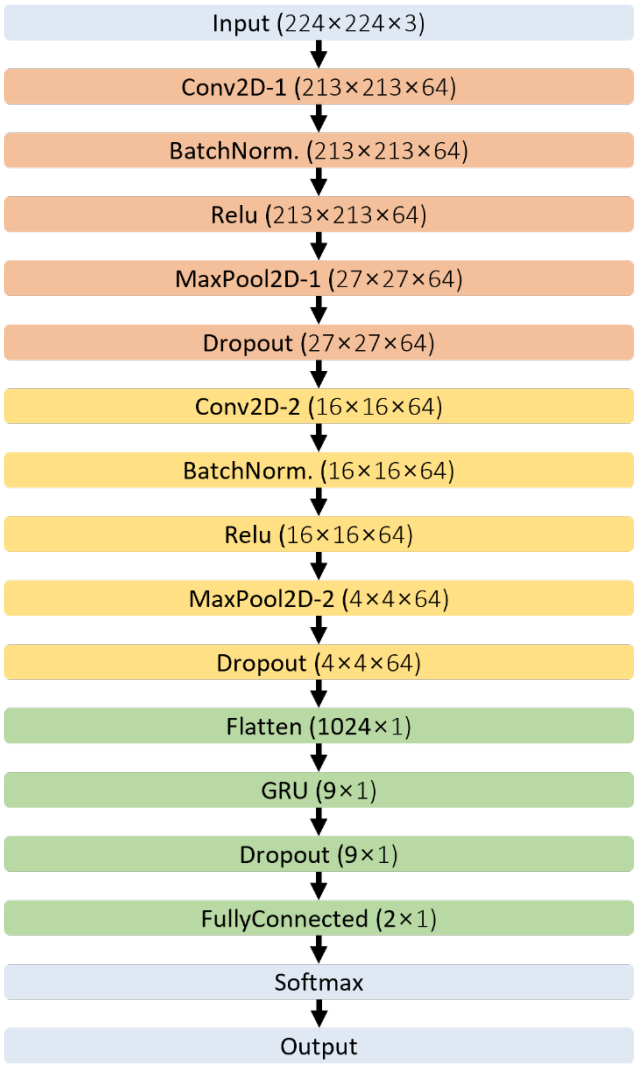

Fig. S14 | Machine learning architecture for apnea detection. The architecture of proposed deep neural network for sleep apnea detection.

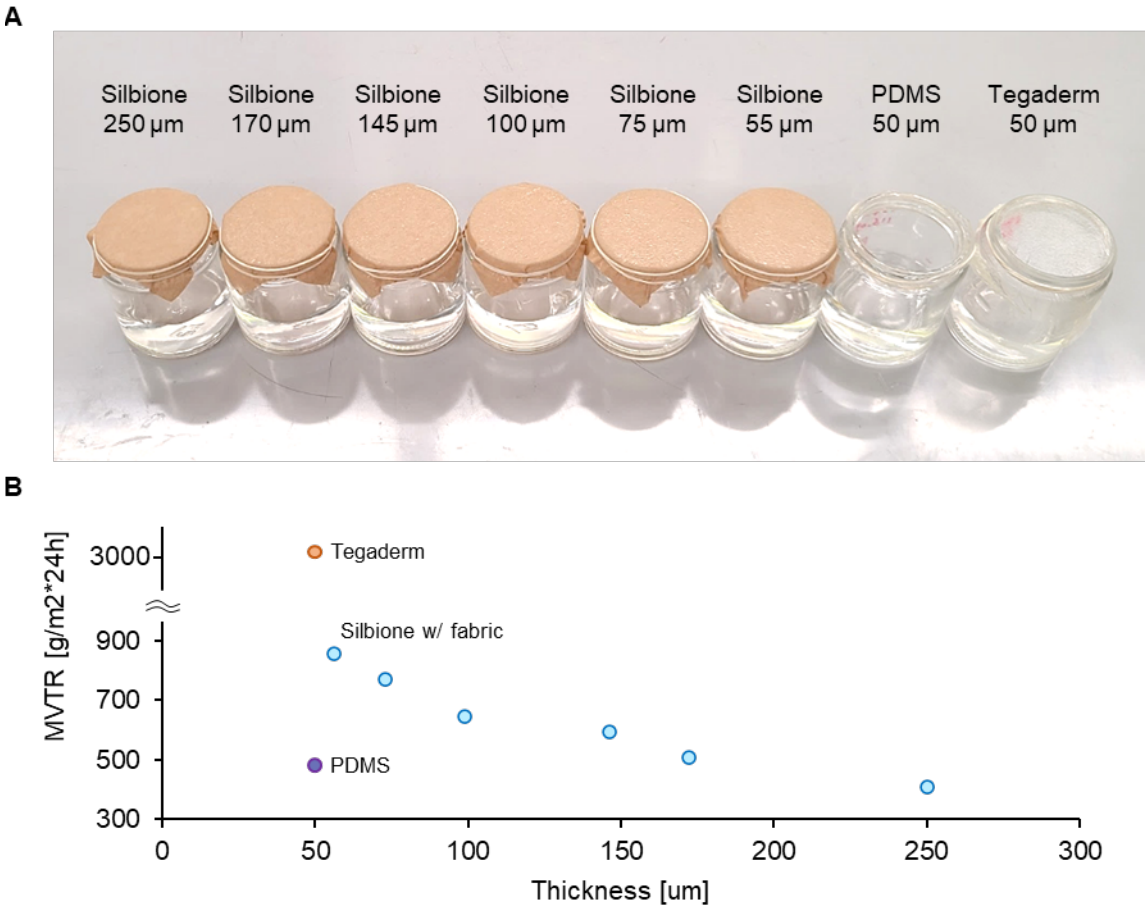

Fig. S15 | MVTR test results (**A**) Test setup: Jars that contain the same amount of water are covered by different cover layers (Fabric brown medical tape with Silbione (55, 75, 100, 145, 170, 250 µm), PDMS (50 µm), Tegarderm (50 µm, 3M)) in the 65℃ oven. (**B**) The plot of MVTR results. Each MVTR value is the average result from 7 days test of each sample.

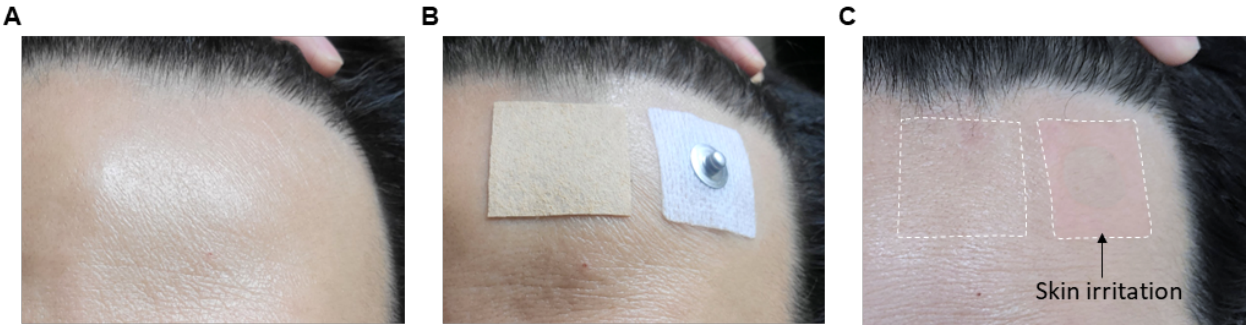

Fig. S16 | Comparison test results wearing the soft patches and commercial get electrodes for 3 days. (**A**) Forehead area before the test. (**B**) Image of fabric electrodes and commercial gel electrodes on the forehead area. (**C**) After 3 days of attachment; No issue in the patch electrodes area. Skin irritated in commercial gel electrodes area.

Table S1 | Machine learning layer information for sleep stage classification. Detailed information about the layers of proposed network for sleep stage classification.

Layer	Output	# filter	Kernel size	Option
Input	256×256×3			
Resize	64×64×3			
Conv2D-1	64×64×112	112	3×3	Stride: 2×2 Mode = Same
BatchNorm	64×64×112			
Leaky_Relu	64×64×112			
MaxPool2D-1	32×32×112		2×2	Stride: 2×2; Mode = Valid
Conv2D-2	32×32×32	32	3×3	Stride: 2×2 Mode = Same
BatchNorm	32×32×32			
Leaky_Relu	32×32×32			
MaxPool2D-2	16×16×32		2×2	Stride: 2×2; Mode = Valid
Conv2D-3	16×16×48	48	5×5	Stride: 2×2 Mode = Same
BatchNorm	16×16×48			
Leaky_Relu	16×16×48			
MaxPool2D-2	8×8×48		2×2	Stride: 2×2; Mode = Valid
Dropout	8×8×48			ρ = 0.45
Flatten	3072×1			
FullyConnected	512×1			
BatchNorm/Dropout	512×1			ρ = 0.45
FullyConnected	64×1			
BatchNorm/Dropout	64×1			ρ = 0.45
Softmax	5×1			
Output	5×1			

Table S2 | Machine learning layer information for apnea detection. Detailed information about the layers of proposed network for sleep apnea detection.

Layer	Output	# filter	Kernel size	Option
Input	224×224×3			
Conv2D-1	213×213×64	64	12×12	Stride: 1×1
BatchNorm	213×213×64			
Relu	213×213×64			
MaxPool2D-1	27×27×64		8×8	Stride: 8×8; Mode=Same
Dropout	27×27×64			ρ = 0.5
Conv2D-1	16×16×64	64	12×12	Stride: 1×1
BatchNorm	16×16×64			
Relu	16×16×64			
MaxPool2D-1	4×4×64		4×4	Stride: 4×4; Mode=Same
Dropout	4×4×64			ρ = 0.5
Flatten	1024×1			
GRU	9×1			Hidden: 9
Dropout	9×1			ρ = 0.5
FullyConnected	2×1			

Table S3 | Sleep stage classification performance comparison of recent EEG-based wearable sleep monitoring devices

Ref.	# of measured signals	# of subjects/classes	Automated scoring algorithm	Classification accuracy of each sleep stage (%)					Overall accuracy (%/kappa)
				W	N1	N2	N3	R	
This work	2 EEG, 2 EOG, 1 EMG	40/5	CNN	88.2	52.3	84.8	86.4	76.9	83.89/0.76
[12]	7 EEG	661/5	LSTM	74.0	47.7	82.9	82.6	84.5	83.5/0.75
[13]	2 EEG, 2 EOG, 1 EMG	1/4	Decision tree	-	-	-	-	-	74/-
[14]	2 EEG, 1 EOG	47/5	Rules and thresholds	80.9	22.9	79.7	74.9	71.5	71.3/0.63
[15]	4 EEG	10/5	SVM	84.1	22.4	85.0	87.1	83.2	76.7/0.69
[17]	8 EEG	20/5	Random forest	83.8	52.0	78.8	92.5	76.7	80.5/0.73
[18]	2 EEG	16/5	SVM	74.3	4.9	84.1	74.7	45.8	74.1/0.61
[19]	18 EEG	15/5	Random forest	-	-	-	-	-	70/0.58

Table S4 | Detail list of electronic components used in circuit design of forehead unit, with description, value, and part number of the corresponding component.

Component	Description	Value	Part Number
U1	1.8V voltage regulator	N/A	TPS62746YFPT
U2	5.0V voltage regulator	N/A	TPS61222DCKR
U3	Bluetooth PSoC	N/A	NRF52832-QFAA-R
U4	ADC with differential amp.	N/A	ADS1299-4PAGR
A1	2.45 GHz RF chip antenna	N/A	2450AT18A100
F1	2.45 GHz low pass filter	N/A	2450FM07A0029
X1	32 MHz crystal	N/A	ECS-320-8-37CKM
X2	32.768 kHz crystal	N/A	ECS-327-9-12-TR
L1	0603 inductor	2.2 μH	N/A
L2	0603 inductor	4.7 μH	N/A
L3	0402 inductor	15 nH	N/A
L4	0603 inductor	10 μH	N/A
L5	0402 inductor	10 nH	N/A
L6	0402 inductor	2.7 nH	N/A
R6, R9, R10	0402 Resistor	1 MΩ	N/A
R14	0402 Resistor	2 kΩ	N/A
C1, C2, C3, C13	0402 ceramic capacitor	10 μF	N/A
C4	0402 ceramic capacitor	1 nF	N/A
C5, C6, C8, C12, C14, C16, C17, C19	0402 ceramic capacitor	1.0 μF	N/A
C7, C9, C18, C11, C20, C22, C26, C31, C32, C33	0402 ceramic capacitor	100 nF	N/A
C10	0603 ceramic capacitor	10 μF	N/A
C15	0603 tantalum capacitor	100 μF	N/A
C21	0402 ceramic capacitor	4.7 μF	N/A
C23	0603 ceramic capacitor	1.0 μF	N/A
C24, C25, C28, C29	0402 ceramic capacitor	12 pF	N/A
C30	0402 ceramic capacitor	1.0 pF	N/A
C34	0402 ceramic capacitor	100 pF	N/A

Table S5 | Detail list of electronic components used in circuit design of chin unit, with description, value and part number of the corresponding component.

Component	Description	Value	Part Number
U1	3.3V voltage regulator	N/A	TPS63001
U2	ADC with differential amp.	N/A	ADS1292IRSMT
U3	Bluetooth PSoC	N/A	NRF52832-QFAA-R
A1	2.45 GHz RF chip antenna	N/A	2450AT18A100
F1	2.45 GHz low pass filter	N/A	2450FM07A0029
X1	32 MHz crystal	N/A	ECS-320-8-37CKM
X2	32.768 kHz crystal	N/A	ECS-327-9-12-TR
L1	0402 inductor	2.2 μH	N/A
L3	0402 inductor	15 nH	N/A
L4	0603 inductor	10 μH	N/A
L5	0402 inductor	10 nH	N/A
L6	0402 inductor	2.7 nH	N/A
R1, R2	0402 Resistor	30 Ω	N/A
R6	0402 Resistor	1 MΩ	N/A
C1, C10	0402 ceramic capacitor	10 μF	N/A
C2	0402 ceramic capacitor	22 μF	N/A
C3, C5	0402 ceramic capacitor	4.7 nF	N/A
C4	0402 ceramic capacitor	1 nF	N/A
C6, C7, C12, C22, C26, C33	0402 ceramic capacitor	100 nF	N/A
C8, C11, C13	0402 ceramic capacitor	1.0 μF	N/A
C9	0402 tantalum capacitor	1.0 μF	N/A
C21	0402 ceramic capacitor	4.7 μF	N/A
C23	0603 ceramic capacitor	1.0 μF	N/A
C24, C25, C28, C29	0402 ceramic capacitor	12 pF	N/A
C30	0402 ceramic capacitor	1.0 pF	N/A
C34	0402 ceramic capacitor	100 pF	N/A

Video S1 shows a device manual that users can easily follow compared to a complicated, time-consuming PSG setup.

Video S2 captures an example of how the wearable system can wirelessly measure EEG, EOG, and chin EMG signals using a table.

Video S3 shows how we utilized a laser to fabricate the critical components of the wearable system.